Advanced active thermography for weld joint inspection

Materials Research Proceedings 57 (2025) 72-79 https://doi.org/10.21741/9781644903735-9

Advanced active thermography for weld joint inspection

Valentino RAZZA[1,3,a *], Manuela DE MADDIS[1,3,b], Pasquale RUSSO SPENA[1,3,c] and Luca SANTORO[2,3,d]

[1]Dipartimento di Ingegneria Gestionale e della Produzione, Politecnico di Torino, Corso Duca degli Abruzzi 24, Torino, Italy

[2]Dipartimento di Ingegneria Meccanica e Aerospaziale, Politecnico di Torino, Corso Duca degli Abruzzi 24, Torino, Italy

[3]J-Tech@PoliTO - Advanced Joining Technologies Laboratory, Politecnico di Torino, Corso Duca degli Abruzzi 24, Torino, Italy

[a]valentino.razza@polito.it, [b]manuela.demaddis@polito.it, [c]pasquale.russospena@polito.it, [d]luca.santoro@polito.it

Keywords: Resistance Welding, Quality Control, Thermography

Abstract. Ensuring the integrity and mechanical performance of critical components is essential in many industrial applications. Widely used inspection methods have several limitations: destructive testing is accurate but involves sample destruction and time-consuming procedures, ultrasonic testing is slow and requires contact and skilled operators, and radiographic testing is expensive and demands stringent safety measures. This work presents an innovative non-destructive inspection method based on active infrared thermography. Modulated heat sources locally heat the specimen while advanced algorithms process the resulting thermal images to generate high-contrast maps for rapid defect detection and material characterization. Its cost-effectiveness and ease of integration into in-line production processes make it highly suitable for automotive, aerospace, and high-precision manufacturing applications.

Introduction

Evaluating weld quality is crucial in manufacturing, as it directly affects the structural integrity and performance of welded components. Conventional inspection methods, such as destructive testing, provide accurate results but lead to significant material waste and require considerable downtime. Nondestructive techniques, such as ultrasonic and radiographic testing, while valuable, are often limited by slow processing speeds, the need for physical contact, complex safety requirements, and the reliance on highly skilled operators [1, 2, 3, 4].

Active thermography has emerged as a powerful alternative in non-destructive testing (NDT). In this technique, an external heat source (e.g., a laser) is used to stimulate the specimen, and an infrared (IR) camera captures the transient thermal response [5, 6, 7, 8, 9]. When combined with a lock-in approach – where the heat source is modulated at a fixed frequency – the method can isolate thermal wave components that are highly sensitive to local variations in thickness, thermal diffusivity, and subsurface defects [10, 11, 12].

In our work, we develop a comprehensive framework for active thermographic inspection that integrates:

- An analytical model of thermal diffusion in a homogeneous slab under laser excitation,
- A gradient-based image processing method to enhance both phase and amplitude contrast in thermal images, and
- An AI-based (transfer learning) model to quantitatively predict microstructural dimensions.

Materials Research Proceedings 57 (2025) 72-79 https://doi.org/10.21741/9781644903735-9

This framework not only produces high-contrast thermal maps for rapid defect detection but also provides quantitative insights into the internal structure of inspected components. Its simplicity, cost-effectiveness, and compatibility with in-line production environments make it an attractive solution for a wide range of industrial applications.

It is worth noting that the present work is still at a feasibility stage, aiming to assess the potential and applicability of the proposed approach. A comprehensive quantitative comparison with existing methodologies, as well as validation on industrial applications, will be addressed in future developments.

Overview on Active Thermography and Frequency Based Approach

Active thermography relies on externally heating the sample and capturing its thermal response over time. In lock-in thermography, the heat source is modulated periodically. For example, when a laser with power $\boldsymbol{P_0}$, having spot radius $\boldsymbol{a}$ and a Gaussian profile defined as a function of the distance $\boldsymbol{r}$ from the spot center excites a slab of thickness $\boldsymbol{\ell}$, the absorbed power is defined as

$$\boldsymbol{P(r) = \eta \frac{P_0}{\pi\, a^2} \exp\left(-\frac{2r^2}{a^2}\right)} \tag{1}$$

where $\boldsymbol{\eta}$ is the power fraction absorbed. The phase delay of the thermal wave at the rear surface is a function of both the material's thermal diffusivity $\boldsymbol{D_s}$ and the modulation frequency $\boldsymbol{f_\ell}$. Under periodic excitation, the phase delay $\boldsymbol{\phi}$ decreases linearly with the distance from the center of the laser spot at a rate of $\boldsymbol{-\ell/\lambda}$, where the thermal diffusion length $\boldsymbol{\lambda}$ is given by

$$\boldsymbol{\lambda = \sqrt{\frac{2D_s}{\omega}}, \quad \omega = 2\pi\, f_\ell.} \tag{2}$$

This relationship shows that even small changes in thickness or thermal diffusivity (due to defects and impurities) can result in measurable phase differences [13].

Lock-in thermography effectively suppresses noise and isolates the oscillatory component, making it suitable for detecting defects in composite materials, metal welds, and other essential structures [10, 11, 12].

The Proposed Methodology: Gradient Method

In our approach, the active thermography experiment generates a series of thermal images $\boldsymbol{T_k^{(r,c)}}$ where $\boldsymbol{k = 0, \dots, N-1}$ denotes the time index and $\boldsymbol{(r, c)}$ represents the pixel coordinates. For each pixel, the temperature signal is analyzed using the Discrete Fourier Transform (DFT)

$$\boldsymbol{\widetilde{T}_n = \sum_{k=0}^{N-1} T_k e^{\frac{i2\pi nk}{N}}, \qquad n = 0, \dots, N-1.} \tag{3}$$

We extract the Fourier coefficient corresponding to the laser modulation frequency, given $\boldsymbol{n\_\ell = \lceil (N\, f\_\ell)/f\_r \rceil}$, and compute its phase as

$$\boldsymbol{\angle \widetilde{T}_{n_\ell} = \operatorname{atan2}\left(\mathrm{I}\{\widetilde{T}_{n_\ell}\}, \Re\{\widetilde{T}_{n_\ell}\}\right).} \tag{4}$$

Due to system delays, an offset $\boldsymbol{\phi_0}$ is present, so the effective phase is

$$\boldsymbol{\phi = \angle \widetilde{T}_{n_\ell} - \phi_0.} \tag{4}$$

Since the ideal theoretical model for a homogeneous slab would yield a smooth phase delay, any local deviations in $\boldsymbol{\phi}$ are indicative of defects or changes in material properties.

Materials Research Proceedings 57 (2025) 72-79 https://doi.org/10.21741/9781644903735-9

An example of such an application can be found in the classification of resistance spot welding (RSW) joints.

In fact, the internal uniformity of the weld spot can be evaluated through statistical indices computed on the phase map (see, e.g., [14]). For instance, we can compute the variance of the phase delay as an internal uniformity index. Moreover, the size of the joint can be estimated from the area in the frame that shows larger heat transfer from the magnitude of $\widetilde{\boldsymbol{T}}_{\mathbf{n}_\ell}$. The contour plot depicted in Figure 1 shows the correlation between the nugget area and phase variance $\boldsymbol{v}$ to the ultimate tensile strength (UTS), highlighting that welds with higher mechanical strength correspond to points with larger nugget areas and lower phase variance. The tests have been performed in different welding conditions:

1. conditions that lead to "bad" spot welds due to a low current value, and thus the presence of an undersized nugget;
2. condition leading to "good" spot welds obtained with the optimized process parameters;
3. condition leading to "bad" spot welds due to high current and the presence of spatter.

To provide information to a non-expert user about the material internal defect, we compute the spatial gradient of the phase map, i.e.,

$$\boldsymbol{\nabla\phi}(\mathbf{x},\mathbf{y}) = \frac{\boldsymbol{\partial\phi}}{\boldsymbol{\partial x}}\hat{\boldsymbol{\imath}} + \frac{\boldsymbol{\partial\phi}}{\boldsymbol{\partial y}}\hat{\boldsymbol{\jmath}}, \tag{5}$$

with the gradient magnitude given by

$$|\boldsymbol{\nabla\phi}(\mathbf{x},\mathbf{y})| = \sqrt{\left(\frac{\boldsymbol{\partial\phi}}{\boldsymbol{\partial x}}\right)^{\mathbf{2}} + \left(\frac{\boldsymbol{\partial\phi}}{\boldsymbol{\partial y}}\right)^{\mathbf{2}}}. \tag{6}$$

Furthermore, to better accentuate radially oriented features (i.e., the weld nugget edges), we compute the vector from each pixel $(\boldsymbol{x},\boldsymbol{y})$ to the weld center $(\boldsymbol{x_c},\boldsymbol{y_c})$

$$\vec{\boldsymbol{c}}\,(\boldsymbol{x},\boldsymbol{y}) = (\boldsymbol{x}-\boldsymbol{x_c})\hat{\boldsymbol{\imath}} + (\boldsymbol{y}-\boldsymbol{y_c})\hat{\boldsymbol{\jmath}}, \tag{7}$$

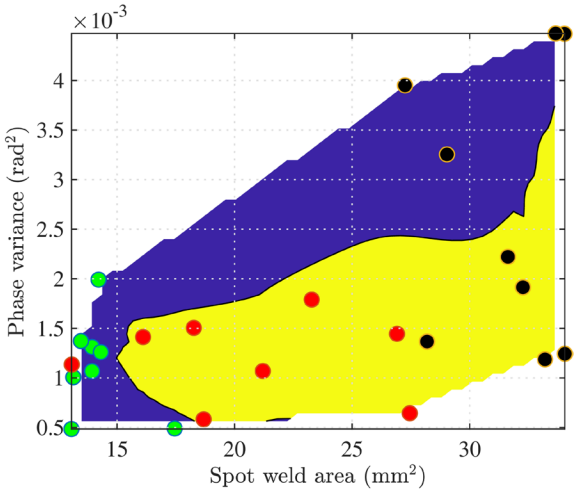

Figure 1: Contour plot relating the thermographic features (nugget area and phase variance) to the ultimate tensile strength (UTS) of the weld. The blue region highlights areas associated with poor-quality welds, defined as those with UTS below 80% of the maximum strength, while the yellow region corresponds to high-quality welds. Dot markers indicate experimentally tested data points from specimen sets 1 (green), 2 (red), and 3 (black)

Materials Research Proceedings 57 (2025) 72-79 https://doi.org/10.21741/9781644903735-9

and define the adjusted gradient magnitude by projecting $\nabla\boldsymbol{\phi}(\mathbf{x},\mathbf{y})$ onto $\vec{\boldsymbol{c}}\,(\boldsymbol{x},\boldsymbol{y})$

$$|\nabla\boldsymbol{\phi}(\mathbf{x},\mathbf{y})|_{\boldsymbol{adj}} = \nabla\boldsymbol{\phi}(\mathbf{x},\mathbf{y})\,\cos\boldsymbol{\theta}(\boldsymbol{x},\boldsymbol{y}), \tag{8}$$

where

$$\cos\boldsymbol{\theta}(\boldsymbol{x},\boldsymbol{y}) = \frac{\nabla\boldsymbol{\phi}(\mathbf{x},\mathbf{y})\cdot\vec{\boldsymbol{c}}\,(\boldsymbol{x},\boldsymbol{y})}{|\nabla\boldsymbol{\phi}(\mathbf{x},\mathbf{y})||\vec{\boldsymbol{c}}\,(\boldsymbol{x},\boldsymbol{y})|}. \tag{9}$$

The gradient-based processing dramatically improves the visualization of the weld features, and it can also be applied to $\left|\widetilde{\boldsymbol{T}}_{\mathbf{n}_\ell}\right|$. Figure 2 shows an example of the magnitude gradient map $\left|\nabla\left|\widetilde{\boldsymbol{T}}_{\mathbf{n}_\ell}\right|\right|$.

A 3D printed PLA plate was used as the test sample, with controlled defects generated in the form of the letters of the "JTech" logo, each embedded in a 1 × 1 cm region at a depth of 0.5 mm. Darker regions indicate higher gradient magnitudes, corresponding to the edges of internal defects. The interested reader finds further details in [15].

Nugget Size Analysis in RSW: Experimental and AI-Assisted Results

The method was used to predict the nugget and corona bond size in resistance spot welding, which is crucial for the quality assurance of the welds.

Notice how the gradient map provides enhanced contrast at the nugget boundary, improving the visualization of the nugget button size (see Figure 3) [16, 17].

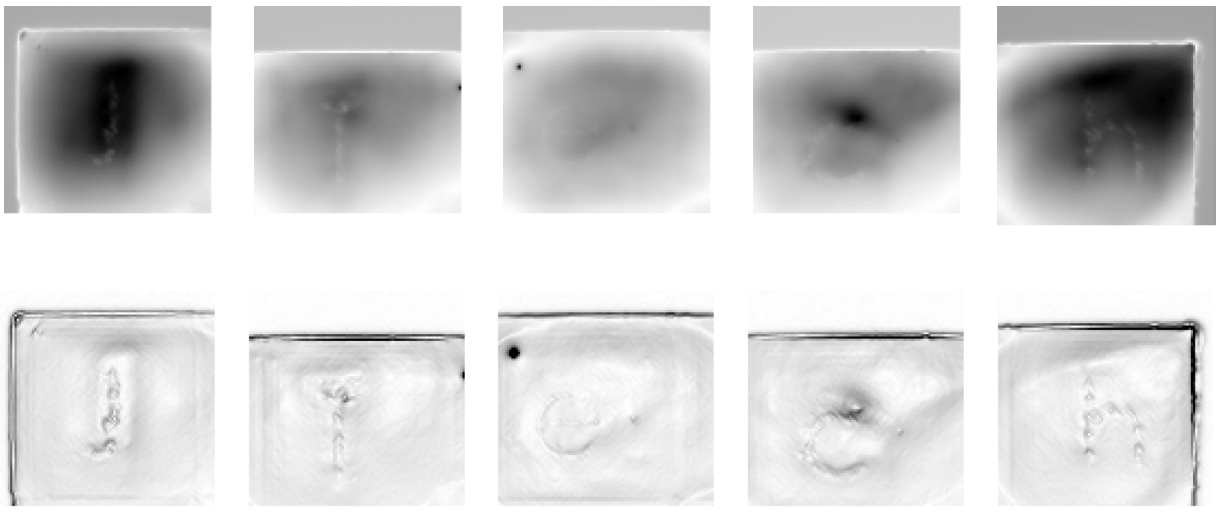

Figure 2: "Jtech" test plate. On the top row, the amplitude map $\left|\widetilde{\boldsymbol{T}}_{\boldsymbol{n}_\ell}\right|$. On the bottom, the amplitude gradient map $\left|\nabla\left|\widetilde{\boldsymbol{T}}_{\boldsymbol{n}_\ell}\right|\right|$.

Materials Research Proceedings 57 (2025) 72-79 https://doi.org/10.21741/9781644903735-9

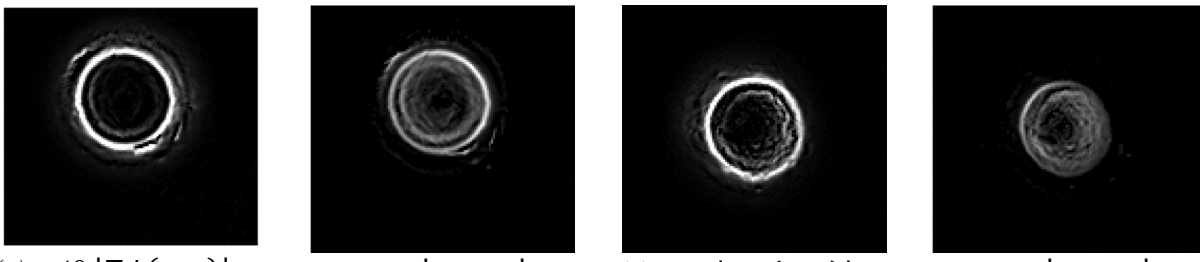

(a) - 48 $|\nabla\phi(x,y)|_{adj}$ (b) - 48 $\left|\nabla|\tilde{\mathbf{T}}_{\mathbf{n}_\ell}|\right|_{adj}$ (c) - 52 $|\nabla\phi(x,y)|_{adj}$ (d) - 48 $\left|\nabla|\tilde{\mathbf{T}}_{\mathbf{n}_\ell}|\right|_{adj}$

Figure 3: Comparison of adjusted maps for different nugget sizes

A convolutional neural network (CNN) further exploits the gradient-based images. Our approach uses a transfer learning model based on the InceptionV3 architecture. The process is as follows

1. *Preprocessing:* The gradient maps from phase and amplitude channels are normalized and converted into three-channel images.
2. *Feature Extraction*: The pre-trained InceptionV3 model acts as a feature extractor.
3. *Regression*: Custom dense layers (with ReLU activation) are appended, and the final output layer (with linear activation) produces a regression estimate of the nugget diameter $\tilde{\boldsymbol{L}}$.

Figure 4 shows the overall CNN architecture used in our study. The network is trained with labeled weld data, and its predictions are compared with metallurgical measurements (see, e.g., [18]). A linear regression model is then used to relate the estimated nugget diameter $\tilde{L}$ to the measured value L as

$$\boldsymbol{L = m\,\tilde{L} + q}, \tag{10}$$

where the regression coefficients m and q are determined via least-squares fitting.

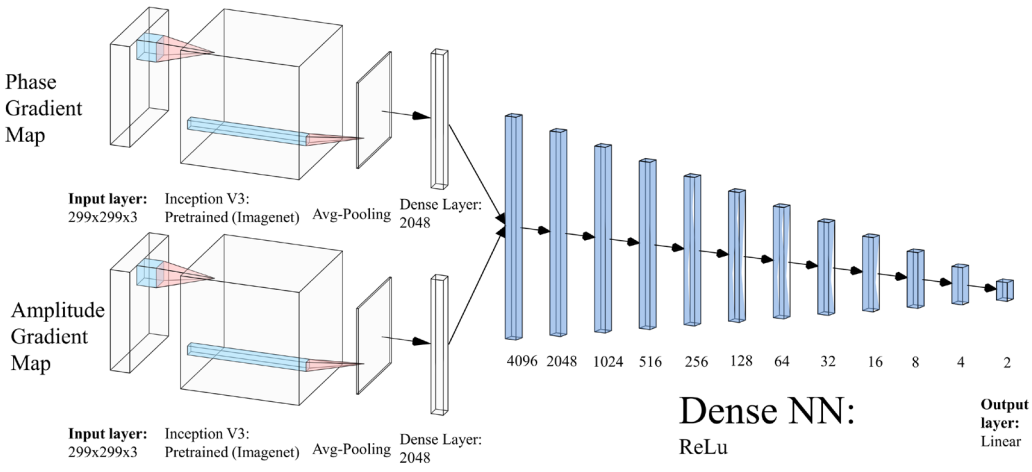

Figure 4: Overview of the CNN architecture based on InceptionV3 used for nugget diameter estimation.

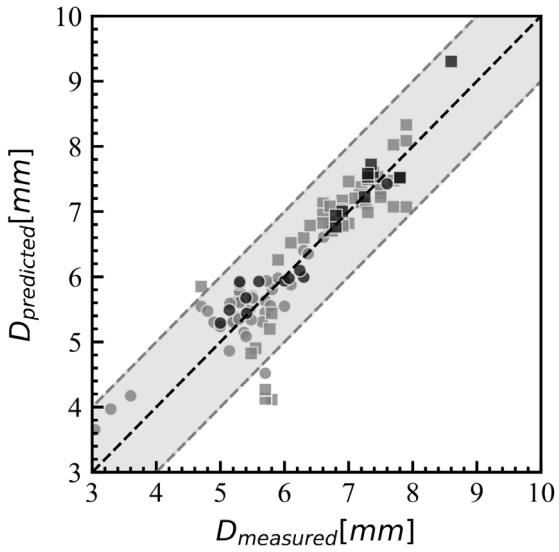

Figure 5: Correlation between AI-predicted nugget diameters $\tilde{\boldsymbol{L}}$ and metallurgical measurements $\boldsymbol{L}$. Gray dots and squares represent nugget and corona bond data from the training set, respectively; black markers correspond to the validation set.

Training a convolutional neural network (CNN) requires a large amount of data that cannot be easily generated from experimental welding tests. It is worth noting that, within the signal processing community, the problem of training reliable CNNs to retrieve info from 2D convolution is a standard procedure in image processing. Thus, we exploit a pre-trained general-purpose image parser neural network, whose output is parsed by a tailored dense neural network (DNN), which provides the nugget and corona bond sizes.

Our experiments yield a Pearson correlation coefficient of 0.94 between the predicted and measured values. Figure 5 shows the correlation between the CNN-predicted nugget sizes and the metallurgical measurements.

Conclusions

In this work, we present a comprehensive methodology for non-destructive evaluation of weld joints using active thermography, combined with gradient-based image processing and artificial intelligence. By employing lock-in thermography, the phase delay, which is highly sensitive to weld thickness and thermal diffusivity, is accurately measured. Subsequent computation of spatial gradients enhances the imaging of weld nugget boundaries and defects. Finally, a CNN leveraging transfer learning from InceptionV3 can predict weld geometrical dimensions with strong correlation to metallurgical measurements.

This integrated approach offers significant promise for automated in-line quality control, reducing the need for destructive testing and enabling more effective process monitoring. Future work will focus on refining the excitation frequency and expanding the dataset to facilitate further validation and improvement of the AI model.

References

[1] T. F. Dahmene, S. Yaacoubi, E. M. Mahjoub, A. E. Bouzenad, P. Rabaey, M. Masmoudi, P. Nennig, T. Dupuy, Y. Benlatreche and A. Taram, "On the nondestructive testing and monitoring of cracks in resistance spot welds: recent gained experience," Welding in the World, vol. 66, no. 4, pp. 629-641, 2022. https://doi.org/10.1007/s40194-022-01249-w

[2] Ó. Martín, M. Pereda, J. I. Santos and J. M. Galán, "Assessment of resistance spot welding quality based on ultrasonic testing and tree-based techniques," Journal of Materials Processing Technology, vol. 214, no. 11, pp. 2478-2487, 2014. https://doi.org/10.1016/j.jmatprotec.2014.05.021

[3] K. Zhou and P. Yao, "Overview of recent advances of process analysis and quality control in resistance spot welding," Mechanical Systems and Signal Processing, vol. 124, pp. 170-198, 2019. https://doi.org/10.1016/j.ymssp.2019.01.041

[4] E. Misokefalou, M. Papoutsidakis and G. Priniotakis, "NON-DESTRUCTIVE TESTING FOR QUALITY CONTROL IN AUTOMOTIVE INDUSTRY," International Journal of Engineering Applied Sciences and Technology, vol. 7, no. 1, pp. 349-355, 2022. https://doi.org/10.33564/IJEAST.2022.v07i01.054

[5] L. Cantini, M. Cucchi, G. Fava and C. Poggi, "Fourier analysis applied to Infrared Thermography of Fiber Composites used for the Strengthening of Structural Elements," in 11th International Conference on Quantitative InfraRed Thermography, 2022.

[6] J. Song, B. Gao, W. L. Woo and G. Y. Tian, "Ensemble tensor decomposition for infrared thermography cracks detection system," Infrared Physics & Technology, vol. 105, p. 103203, 2020. https://doi.org/10.1016/j.infrared.2020.103203

[7] N. Rajic, "Principal component thermography for flaw contrast enhancement and flaw depth characterisation in composite structures," Composite Structures, vol. 58, no. 4, pp. 521-528, 2002. https://doi.org/10.1016/S0263-8223(02)00161-7

[8] K.-L. Huang, S. Sfarra, C.-M. Wen, Y. Yao and C. Zhao, "Exploratory factor analysis for defect identification with active thermography," Measurement Science and Technology, vol. 32, no. 11, p. 114010, 2021. https://doi.org/10.1088/1361-6501/ac17f9

[9] C. Maierhofer, M. Röllig, H. Steinfurth, M. Ziegler, M. Kreutzbruck, C. Scheuerlein and S. Heck, "Non-destructive testing of Cu solder connections using active thermography," NDT & E International, vol. 52, pp. 103-111, 2012. https://doi.org/10.1016/j.ndteint.2012.07.010

[10] K. Strzałkowski, M. Streza, D. Dadarlat and A. Marasek, "Thermal characterization of II-VI binary crystals by photopyroelectric calorimetry and infrared lock-in thermography," Journal of Thermal Analysis and Calorimetry, vol. 119, no. 1, pp. 319-327, 2015. https://doi.org/10.1007/s10973-014-4137-0

[11] A. Mendioroz, R. Fuente-Dacal, E. Apiñaniz and A. Salazar, "Thermal diffusivity measurements of thin plates and filaments using lock-in thermography," Review of Scientific Instruments, vol. 80, no. 7, p. 074904, 2009. https://doi.org/10.1063/1.3176467

[12] A. Philipp, N. W. Pech-May, B. A. F. Kopera, A. M. Lechner, S. Rosenfeldt and M. Retsch, "Direct Measurement of the In-Plane Thermal Diffusivity of Semitransparent Thin Films by Lock-In Thermography: An Extension of the Slopes Method," Analytical Chemistry, vol. 91, no. 13, pp. 8476-8483, 2019. https://doi.org/10.1021/acs.analchem.9b01583

[13] H. Kato, T. Baba and M. Okaji, "Anisotropic thermal-diffusivity measurements by a new laser-spot-heating technique," Measurement Science and Technology, vol. 12, no. 12, p. 2074, 2001. https://doi.org/10.1088/0957-0233/12/12/307

[14] L. Santoro, V. Razza and M. De Maddis, "Frequency-based analysis of active laser thermography for spot weld quality assessment," International Journal of Advanced Manufacturing Technology, 2023. https://doi.org/10.1007/s00170-023-12845-5

[15] V. Razza, L. Santoro and M. De Maddis, "Gradient-based image generation for thermographic material inspection," Applied Thermal Engineering, vol. 268, p. 125900, 2025. https://doi.org/10.1016/j.applthermaleng.2025.125900

[16] Á. Cifuentes, A. Mendioroz and A. Salazar, "Simultaneous measurements of the thermal diffusivity and conductivity of thermal insulators using lock-in infrared thermography," International Journal of Thermal Sciences, vol. 121, pp. 305-312, 2017. https://doi.org/10.1016/j.ijthermalsci.2017.07.023

[17] L. Santoro, R. Sesana, R. Molica Nardo and F. Curà, "Infrared in-line monitoring of flaws in steel welded joints: a preliminary approach with SMAW and GMAW processes," International Journal of Advanced Manufacturing Technology, 2023. https://doi.org/10.1007/s00170-023-12044-2

[18] L. Santoro, V. Razza and M. De Maddis, "Nugget and corona bond size measurement through active thermography and transfer learning model," International Journal of Advanced Manufacturing Technology, vol. 133, no. 11, pp. 5883-5896, 2024. https://doi.org/10.1007/s00170-024-14096-4